nature astronomy

Supplementary information https://doi.org/10.1038/s41550-025-02513-x

SiO and a super-stellar C/O ratio in the atmosphere of the giant exoplanet WASP-121 b

In the format provided by the authors and unedited

Supplementary Table 1 | White phase-curve fit results. Posterior distributions (medians with 1σ uncertainties defined by the 16th and 84th percentiles of $n = 5{,}000$ posterior samples) and best-fit values for the fitted and derived phase-curve model parameters.

Fitted parameters	Posterior distribution	Best-fit
Shared: $M_\star$ ($M_\odot$)	$1.332^{+0.018}_{-0.017}$	1.332
Shared: M_p (M_J)	$1.168^{+0.040}_{-0.041}$	1.170
Shared: i (°)	$87.97^{+0.17}_{-0.15}$	87.96
Shared: log₁₀[$R_\star$ ($R_\odot$)]	$0.1567^{+0.0020}_{-0.0020}$	0.1567
Shared: ΔP_orb (sec)	$-0.0009^{+0.0129}_{-0.0121}$	−0.0009
NRS1: log₁₀[R_p (R_J)]	$0.233^{+0.002}_{-0.002}$	0.233
NRS2: log₁₀[R_p (R_J)]	$0.237^{+0.002}_{-0.002}$	0.237
NRS1: ΔT_mid (sec)	-26^{+17}_{-18}	−26
NRS2: ΔT_mid (sec)	-28^{+17}_{-18}	−28
NRS1: A (ppm)	2031^{+6}_{-7}	2031
NRS2: A (ppm)	2784^{+8}_{-9}	2784
NRS1: $y_{1,0}$	$0.804^{+0.003}_{-0.003}$	0.805
NRS2: $y_{1,0}$	$0.669^{+0.002}_{-0.002}$	0.669
NRS1: $\Delta\phi$ (°)	$2.95^{+0.11}_{-0.12}$	2.96
NRS2: $\Delta\phi$ (°)	$2.39^{+0.12}_{-0.13}$	2.39
NRS1: u_1	$0.048^{+0.006}_{-0.006}$	0.047
NRS2: u_1	$0.031^{+0.005}_{-0.006}$	0.030
NRS1: u_2	$0.118^{+0.010}_{-0.011}$	0.120
NRS2: u_2	$0.090^{+0.010}_{-0.009}$	0.090

Supplementary Table 1 ***(continued)***

Derived parameters	Posterior distribution	Best-fit
Shared: $R_\star$ ($R_\odot$)	$1.434^{+0.007}_{-0.007}$	1.434
NRS1: R_p (R_J)	$1.712^{+0.008}_{-0.008}$	1.721
NRS2: R_p (R_J)	$1.727^{+0.008}_{-0.008}$	1.727
NRS1: $R_\mathrm{p}/R_\star$	$0.122659^{+0.000062}_{-0.000056}$	0.122657
NRS2: $R_\mathrm{p}/R_\star$	$0.123732^{+0.000064}_{-0.000066}$	0.123736
Shared: ΔP_orb (day)	$1.27492503^{+0.00000015}_{-0.00000014}$	1.27492503
NRS1: ΔT_mid (BJD_{TDB})	$2459867.64267^{+0.00020}_{-0.00021}$	2459867.64265
NRS2: ΔT_mid (BJD_{TDB})	$2459867.64265^{+0.00020}_{-0.00021}$	2459867.64263

Supplementary Table 2 | Atmospheric opacities. Line and continuum opacity sources used by each retrieval code. Note that the abundances for TiO, VO, FeH, HCN, NH_3, C_2H_2 and OH were held fixed to values appropriate for a background solar composition atmosphere in the PETRA retrieval, including the opacity sources listed for the PHOENIX model in Extended Data Table 2 of ref. [58]. For further details on opacity sources adopted by the ATMO retrieval, which assumed thermochemical equilibrium including additional species not shown below, see refs [60-64].

Opacity	ATMO	NEMESIS	HyDRA	CHIMERA	PETRA
H_2O	72	73	74	73	72
CH_4	75	76	75, 77	78	—
CO	74	79	74	74	80
SiO	81	81	82	—	83
CO_2	84	85	74	85	86
SiO_2	—	—	87	—	—
HCN	88,89	89	88	89	86
NH3	90	—	—	91	86
C_2H_2	92	93	—	93	86
H^-	94, 95	94	94, 95	—	94
H_2-H_2	96	97, 98	96	96	99
H_2-He	96	100, 101	96	96	99
OH	—	—	74	—	86
TiO	102	—	103	—	104
VO	105	—	105	—	106
FeH	107	—	108	—	108

Supplementary Table 3 | Priors adopted for the ATMO retrievals. Listed values give the lower and upper bounds of the uniform distributions used as priors in the retrieval analyses.

ATMO dayside			ATMO nightside		
Parameter	**Description**	**Prior**	**Parameter**	**Description**	**Prior**
[C/H]	Carbon Metallicity	$[-1, 2]$ dex	[C/H]	Carbon metallicity	$[-1, 2]$ dex
[O/H]	Oxygen metallicity	$[-1, 2]$ dex	[O/H]	Oxygen metallicity	$[-1, 2]$ dex
[Si/H]	Silicon metallicity	$[-1, 2]$ dex	[Si/H]	Silicon metallicity	$[-1, 2]$ dex
[M/H]	Other heavy elements metallicity	$[-1, 2]$ dex	[M/H]	Other heavy elements metallicity	$[-1, 2]$ dex
$\log_{10} \kappa_{\mathrm{IR}}$	Infrared opacity	$[-5, -0.5]$ dex	$\log_{10} \kappa_{\mathrm{IR}}$	Infrared opacity	$[-5, -0.5]$ dex
$\log_{10} \gamma_{\mathrm{V1/IR}}$	Visible channel 1 relative opacity	$[-4, 1.5]$ dex	$\log_{10} \gamma_{\mathrm{V/IR}}$	Visible Relative opacity	$[-4, 1.5]$ dex
$\log_{10} \gamma_{\mathrm{V2/IR}}$	Visible channel 2 relative opacity	$[-4, 1.5]$ dex	β_{r}	Redistribution factor	$[0, 2]$
β_{r}	Redistribution factor	$[0, 2]$			
α_{V}	Visible channels partition	$[0, 1]$			

Supplementary Table 4 | Priors adopted for the NEMESIS retrievals. The same as Supplementary Table 3, for the NEMESIS retrievals.

NEMESIS dayside			NEMESIS nightside		
Parameter	**Description**	**Prior**	**Parameter**	**Description**	**Prior**
$\log_{10}$ H_2O	Log H_2O deep mixing ratio	$[-12, -1]$ dex	$\log_{10}$ H_2O	Log H_2O mixing ratio	$[-12, -1]$ dex
$\log_{10} P_0$	Log H_2O knee pressure	$[-12, -1]$ dex	$\log_{10}$ H^-	Log H^- mixing ratio	$[-13, -5]$ dex
$\log_{10} \tau$	Log H_2O power index	$[-12, -1]$ dex	$\log_{10}$ CO	Log CO mixing ratio	$[-12, -1]$ dex
$\log_{10}$ H^-	Log H^- mixing ratio	$[-13, -5]$ dex	$\log_{10}$ CO_2	Log CO_2 mixing ratio	$[-12, -1]$ dex
$\log_{10}$ CO	Log CO mixing ratio	$[-12, -1]$ dex	$\log_{10}$ CH_4	Log CH_4 mixing ratio	$[-12, -1]$ dex
$\log_{10}$ CO_2	Log CO_2 mixing ratio	$[-12, -1]$ dex	$\log_{10}$ SiO	Log SiO mixing ratio	$[-12, -1]$ dex
$\log_{10}$ CH_4	Log CH_4 mixing ratio	$[-12, -1]$ dex	$\log_{10}$ C_2H_2	Log C_2H_2 mixing ratio	$[-12, -1]$ dex
$\log_{10}$ SiO	Log SiO mixing ratio	$[-12, -1]$ dex	$\log_{10}$ HCN	Log HCN mixing ratio	$[-12, -1]$ dex
$\log_{10} P_1$	Log PT pressure 1	$[-8, 2]$ dex bar	$\log_{10} P_1$	Log PT pressure 1	$[-8, 2]$ dex bar
$\log_{10} P_2$	Log PT pressure 2	$[-8, 2]$ dex bar	$\log_{10} P_2$	Log PT pressure 2	$[-8, 2]$ dex bar
$\log_{10} P_3$	Log PT pressure 3	$[-8, 2]$ dex bar	$\log_{10} P_3$	Log PT pressure 3	$[-8, 2]$ dex bar
T_1	Temperature at P_1	$[1000, 3500]$ K	T_1	Temperature at P_1	$[800, 3300]$ K
α_1	PT power index 1	$[0.02, 1]$	α_1	PT power index 1	$[0.02, 1]$
α_2	PT power index 2	$[0.02, 1]$	α_2	PT power index 2	$[0.02, 1]$
			$\log_{10} P_{\text{top}}$	Log cloud pressure	$[-6, 1]$ dex bar
			γ	Scattering index	$[0, 14]$
			σ_0	Log cloud opacity	$[-10, 10]$ dex

Supplementary Table 5 | Priors adopted for the CHIMERA retrievals. The same as Supplementary Tables 3-4, for the CHIMERA retrievals.

CHIMERA nightside		
Parameter	**Description**	**Prior**
$\log_{10}$ H_2O	Log H_2O mixing ratio	$[-12, -1]$ dex
$\log_{10}$ CO	Log CO mixing ratio	$[-12, -1]$ dex
$\log_{10}$ CO_2	Log CO_2 mixing ratio	$[-12, -1]$ dex
$\log_{10}$ CH_4	Log CH_4 mixing ratio	$[-12, -1]$ dex
$\log_{10}$ C_2H_2	Log C_2H_2 mixing ratio	$[-12, -1]$ dex
$\log_{10}$ HCN	Log HCN mixing ratio	$[-12, -1]$ dex
$\log_{10}$ NH_3	Log NH_3 mixing ratio	$[-12, -1]$ dex
$\log_{10} \kappa_{\mathrm{IR}}$	Infrared opacity	$[-4, 2.5]$ dex
$\log_{10} \gamma_{\mathrm{V1/IR}}$	Visible channel 1 relative opacity	$[-2.5, 4]$ dex
$\log_{10} \gamma_{\mathrm{V2/IR}}$	Visible channel 2 relative opacity	$[-2.5, 4]$ dex
T_{eff}	Effective temperature	$[400, 2800]$ K
α_{V}	Visible channels partition	$[0, 1]$
δ	Dilution factor	$[0, 1]$

Supplementary Table 6 | Priors adopted for the HyDRA retrievals. The same as Supplementary Tables 3-5, for the HyDRA retrievals.

HyDRA dayside			HyDRA nightside		
Parameter	**Description**	**Prior**	**Parameter**	**Description**	**Prior**
$\log_{10}$ H_2O	Log H_2O deep mixing ratio	$[-15, -1]$ dex	$\log_{10}$ H_2O	Log H_2O mixing ratio	$[-15, -1]$ dex
$\log_{10}$ H^-	Log H^- mixing ratio	$[-15, -1]$ dex	$\log_{10}$ H^-	Log H^- mixing ratio	$[-15, -1]$ dex
$\log_{10}$ CO	Log CO mixing ratio	$[-15, -1]$ dex	$\log_{10}$ CO	Log CO mixing ratio	$[-15, -1]$ dex
$\log_{10}$ CO_2	Log CO_2 mixing ratio	$[-15, -1]$ dex	$\log_{10}$ CO_2	Log CO_2 mixing ratio	$[-15, -1]$ dex
$\log_{10}$ SiO	Log SiO mixing ratio	$[-15, -1]$ dex	$\log_{10}$ CH_4	Log CH_4 mixing ratio	$[-15, -1]$ dex
$\log_{10}$ SiO_2	Log SiO_2 mixing ratio	$[-15, -1]$ dex	$\log_{10}$ SiO	Log SiO mixing ratio	$[-15, -1]$ dex
$\log_{10}$ TiO	Log TiO mixing ratio	$[-15, -1]$ dex	$\log_{10}$ SiO_2	Log SiO_2 mixing ratio	$[-15, -1]$ dex
$\log_{10}$ VO	Log VO mixing ratio	$[-15, -1]$ dex	$\log_{10}$ HCN	Log HCN mixing ratio	$[-15, -1]$ dex
$\log_{10}$ OH	Log OH mixing ratio	$[-15, -1]$ dex	$\log_{10} P_1$	Log PT pressure 1	$[-5, 3]$ dex bar
$\log_{10}$ FeH	Log FeH mixing ratio	$[-15, -1]$ dex	$\log_{10} P_2$	Log PT pressure 2	$[-5, 3]$ dex bar
$\log_{10}$ HCN	Log HCN mixing ratio	$[-15, -1]$ dex	$\log_{10} P_3$	Log PT pressure 3	$[-5, 3]$ dex bar
$\log_{10} P_1$	Log PT pressure 1	$[-5, 3]$ dex bar	T_1	100 mbar temperature	$[500, 4000]$ K
$\log_{10} P_2$	Log PT pressure 2	$[-5, 3]$ dex bar	α_1	PT power index 1	$[0.02, 1]$
$\log_{10} P_3$	Log PT pressure 3	$[-5, 3]$ dex bar	α_2	PT power index 2	$[0.02, 1]$
T_1	100 mbar temperature	$[500, 4000]$ K	δ	Dilution factor	$[0, 1]$
α_1	PT power index 1	$[0.02, 1]$	$\log_{10} a_c$	Modal cloud particle size	$[-2, 1]$ dex
α_2	PT power index 2	$[0.02, 1]$	$\log_{10} P_c$	Cloud base pressure	$[-5, 2]$ dex bar
δ	Dilution factor	$[0, 1]$	$\log_{10} f_c$	Cloud particle abundance	$[-30, -1]$ dex
$\log_{10} a_c$	Modal cloud particle size	$[-2, 1]$ dex	ε	Cloud pressure exponent	$[0.3, 10]$
$\log_{10} P_c$	Cloud base pressure	$[-5, 2]$ dex bar	ψ_c	Cloud covering fraction	$[0, 1]$
$\log_{10} f_c$	Cloud particle abundance	$[-30, -1]$ dex			

Supplementary Table 6 ***(continued)***

ε	Cloud pressure exponent	$[\,0.3, 10\,]$			
ψ_c	Cloud covering fraction	$[\,0, 1\,]$			

Supplementary Table 7 I Priors adopted for the PETRA retrievals. The same as Supplementary Tables 3-6, for the PETRA retrievals.

PETRA dayside		
Parameter	**Description**	**Prior**
$\log_{10}$ H_2O	Log H_2O deep mixing ratio	$[-20, -1\,]$ dex
$\log_{10} P_0$	Log H_2O knee pressure	$[-5, 5\,]$ dex bar
$\log_{10} \tau$	Log H_2O power index	$[-15, 15\,]$ dex
$\log_{10}$ CO	Log CO mixing ratio	$[-20, -1\,]$ dex
$\log_{10}$ SiO	Log SiO mixing ratio	$[-20, -1\,]$ dex
$\log_{10} \kappa_{IR}$	Infrared opacity	$[\,-4, 2.5\,]$ dex
$\log_{10} \gamma_{V1/IR}$	Visible channel 1 relative opacity	$[-2.5, 4\,]$ dex
$\log_{10} \gamma_{V2/IR}$	Visible channel 2 relative opacity	$[-2.5, 4\,]$ dex
β_r	Redistribution factor	$[\,0.3, 1.75\,]$
α_V	Visible channels partition	$[\,0, 1\,]$

Supplementary Table 8 I Stellar atomic data, equivalent-width measurements, and individual line abundance inferences. In columns one through five we give the wavelength of the atomic transition, the species, excitation potential of the transition (ep), the logarithm of the transition probability (log(gf)), the measured equivalent width (EW) and the calculated line abundance (A(X)), respectively. The atomic data are an updated version of the line list initially presented in ref. [151], with the addition of hyperfine structure and isotopic splitting for several elements. *Provided as a Supplementary File in .xlsx format.*

Supplementary Table 9 | Properties of the WASP-121 host star. All of our stellar parameters were inferred with the methodology described in ref. [138], which is a hybrid of classical spectroscopic analysis and an isochrone fitting technique, with the spectroscopic data being used as a prior to the isochrone fitting. Quoted values are the medians with 1σ uncertainties defined by the 16th and 84th percentiles. With our methodology the inferred stellar parameters are consistent with all available stellar information, namely: spectroscopic, photometric, astrometric and extinction data. Effective temperature is derived mostly from photometric information, surface gravity comes mostly from astrometric data, and metallicity from spectroscopic data.

Parameter	Value	Unit
Tycho *B*	11.093 ± 0.049	Vega mag
Tycho *V*	10.571 ± 0.045	Vega mag
Gaia DR2 *G*	10.3752 ± 0.002	Vega mag
2MASS *J*	9.625 ± 0.021	Vega mag
2MASS *H*	9.439 ± 0.025	Vega mag
2MASS K_s	9.374 ± 0.022	Vega mag
WISE W_1	9.356 ± 0.023	Vega mag
WISE W_2	9.387 ± 0.019	Vega mag
Gaia DR3 parallax	3.799 ± 0.010	mas
Distance, *d*	$262.6^{+0.3}_{-0.5}$	pc
Interstellar extinction, A_V	$0.05^{+0.02}_{-0.03}$	mag
Effective temperature, T_{eff}	6481^{+46}_{-48}	K
Surface gravity, $\log_{10} g_\star$	$4.23^{+0.01}_{-0.02}$	dex m/s^2
Stellar mass, $M_\star$	$1.36^{+0.03}_{-0.03}$	$M_\odot$
Stellar radius, $R_\star$	$1.49^{+0.01}_{-0.01}$	$R_\odot$
Luminosity, $L_\star$	3.52 ± 0.08	$L_\odot$
Isochrone-based age, t_{iso}	$1.65^{+0.35}_{-0.33}$	Gyr
Metallicity, [Fe/H]	0.114 ± 0.039	dex
Microturbulence, ξ	1.57 ± 0.11	km/s

Supplementary Table 10 | WASP-121 stellar abundances. Mean estimated abundances for each of our measured elements in standard [X/H] and *A*(X) formats, where *A*(X) = $\log_{10} N_X/N_H + 12$. Quoted uncertainties include both the line-by-line dispersion when multiple lines were available, and uncertainties propagated from the stellar parameter uncertainties. Non-LTE corrections obtained using a multi-variable linear interpolation technique are provided where available, with uncertainties reflecting the line-by-line dispersion.

	LTE abundances		**Non-LTE abundances**	
Species	**[X/H]**	***A*(X)**	**[X/H]**	***A*(X)**
C I	0.085 ± 0.063	8.545 ± 0.063	0.067 ± 0.050	8.527 ± 0.050
O I	0.548 ± 0.052	9.238 ± 0.052	0.165 ± 0.024	8.855 ± 0.024
Na I	0.172 ± 0.029	6.392 ± 0.029	—	—
Mg I	0.046 ± 0.147	7.596 ± 0.147	—	—
Al I	0.110 ± 0.030	6.540 ± 0.030	0.096	6.526
Si I	0.201 ± 0.037	7.711 ± 0.037	0.195 ± 0.097	7.696 ± 0.097
S I	0.144 ± 0.117	7.264 ± 0.117	—	—
K I	0.616 ± 0.084	5.686 ± 0.084	0.099	5.169
Ca I	0.212 ± 0.056	6.512 ± 0.056	-0.304 ± 0.111	5.996 ± 0.111
Ti II	0.107 ± 0.079	5.077 ± 0.079	—	—
V I	-0.064 ± 0.063	3.836 ± 0.063	—	—
Cr I	0.166 ± 0.071	5.786 ± 0.071	—	—
Cr II	0.230 ± 0.088	5.850 ± 0.088	—	—
Mn I	0.016 ± 0.060	5.436 ± 0.060	—	—
Fe I	0.126 ± 0.044	7.586 ± 0.044	0.164 ± 0.079	7.624 ± 0.079
Fe II	0.169 ± 0.070	7.629 ± 0.070	0.221 ± 0.075	7.681 ± 0.075
Co I	0.132 ± 0.035	5.072 ± 0.035	—	—
Ni I	0.150 ± 0.051	6.350 ± 0.051	—	—
Cu I	0.021 ± 0.091	4.201 ± 0.091	—	—
Zn I	-0.021 ± 0.057	4.539 ± 0.057	—	—
Sc II	0.269 ± 0.099	3.409 ± 0.099	—	—

Supplementary Table 10 ***(continued)***

Y II	0.233 ± 0.146	2.443 ± 0.146	—	—
Zr II	0.051 ± 0.113	2.641 ± 0.113	—	—
Ba II	0.166 ± 0.127	2.436 ± 0.127	—	—
Ce II	0.212 ± 0.117	1.792 ± 0.117	—	—
Nd II	0.308 ± 0.067	1.728 ± 0.067	—	—
Sm II	0.344 ± 0.066	1.294 ± 0.066	—	—

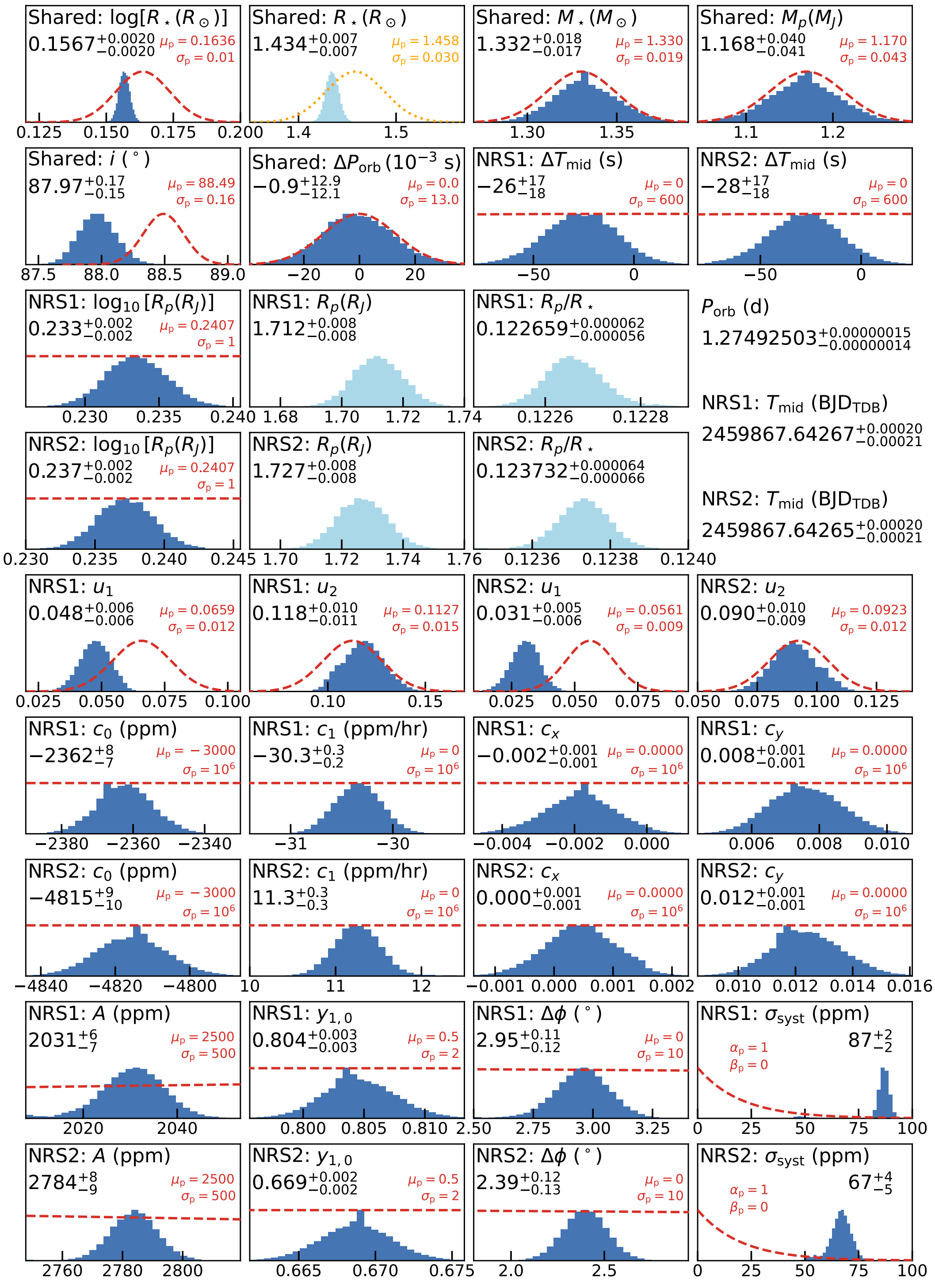

Supplementary Fig. 1 | Results of the white phase-curve fit. An updated version of a similar figure presented in ref. [5]. Dark (light) blue histograms show posterior distributions for fitted (derived) parameters. Posterior median values with 1σ uncertainties defined by the 16th and 84th percentiles of $n = 5{,}000$ posterior samples are displayed in black font. Prior distributions are plotted as dashed red lines, with corresponding parameters displayed in red font, namely: the mean (μ_{p}) and standard deviation (σ_{p}) for normal priors; and the shape (α_{p}) and inverse-scale (β_{p}) parameters for gamma priors. Our derived distribution for $R_\star$ is compared to the posterior distribution for the stellar radius reported by ref. [56], which is shown by the dotted orange line.

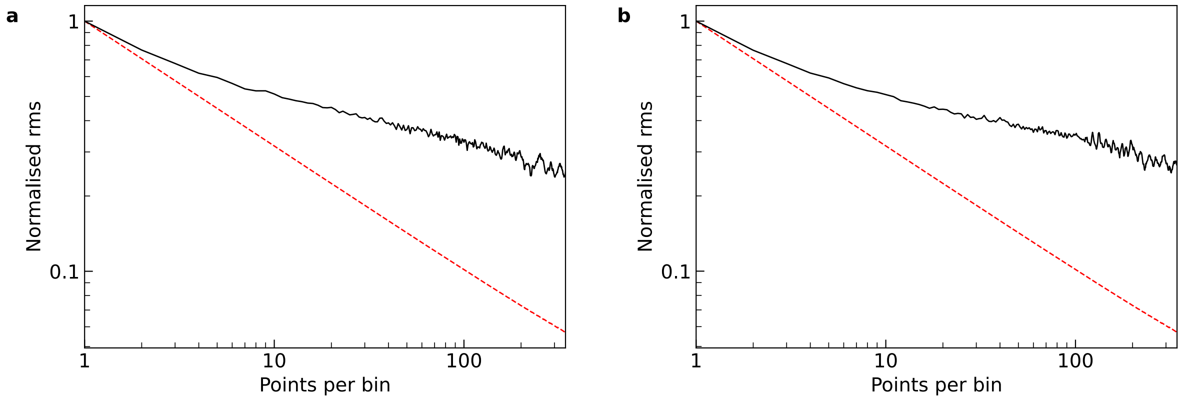

Supplementary Fig. 2 | Root mean square (rms) of white phase-curve model residuals. **a,** The black line shows how the normalised rms of the best-fit model residuals bins down as a function of the number of points per bin for the NRS1 white phase curve. The dashed red line indicates the expected rms scaling for uncorrelated ('white') noise. **b,** The same as **a**, but for the NRS2 white phase-curve fit.

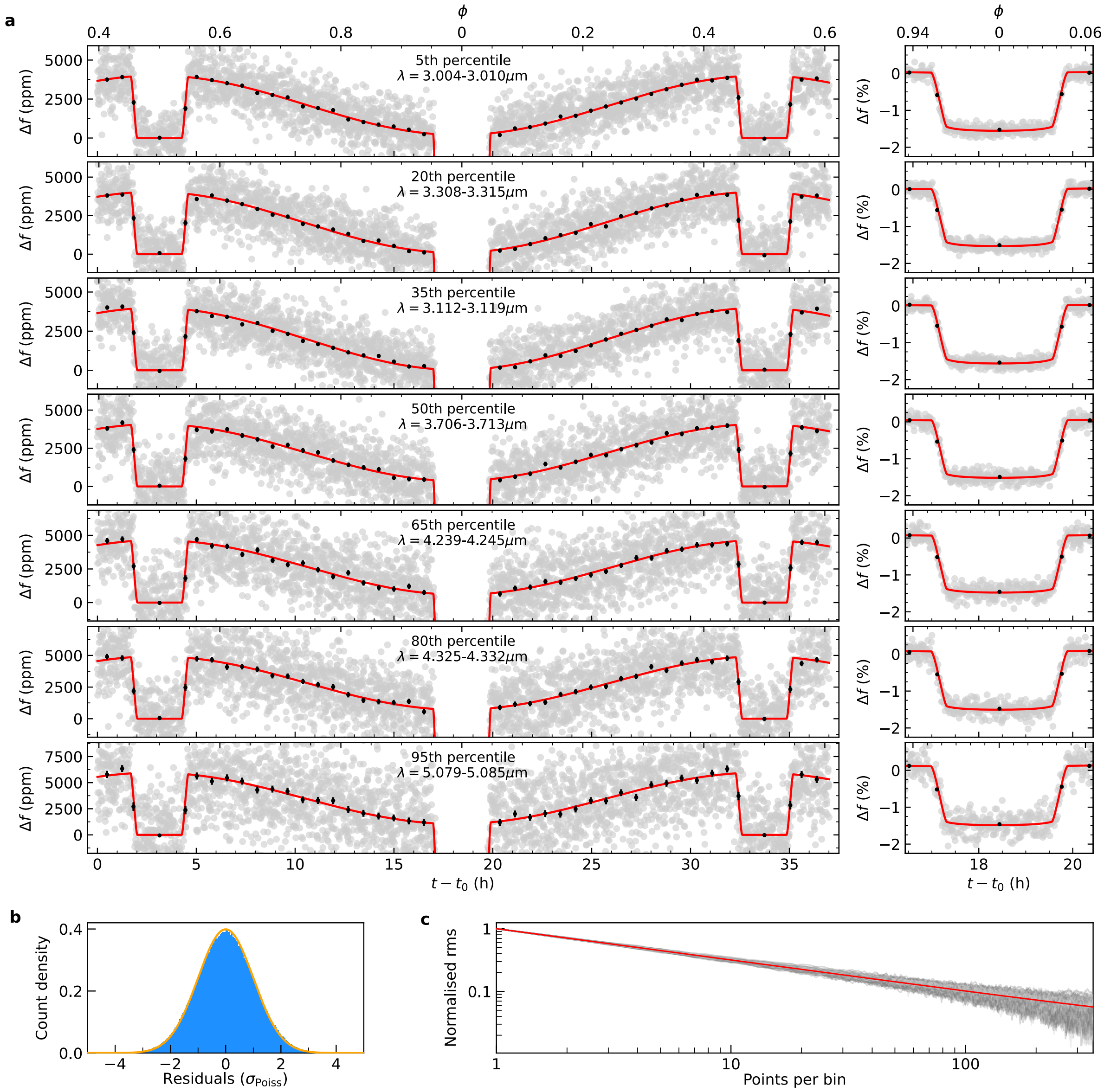

Supplementary Fig. 3 | Spectroscopic phase-curve fits and residuals. a, A selection of spectroscopic phase curves illustrating the range of fit qualities across all wavelength channels, ranging from the 5th to 95th percentiles as measured by the χ^2 statistic. The left column highlights the planetary emission component of the signal and the right column gives a close-up of the primary transit. Grey circles are the measured emission relative to the stellar baseline level (Δf), after correcting for the instrument baseline trend and subtracting the stellar baseline level. Black circles show median values and error bars indicate standard deviations (1σ uncertainties) based on $n = 5{,}000$ posterior samples, for the phase bins used to generate the phase-resolved emission spectra, as well as additional bins for the ingress, bottom and egress of the primary transit and each secondary eclipse. Red lines show the best-fit phase-curve models. **b,** Blue bars show a histogram of the binned model residuals for all spectroscopic phase curves, expressed in units of the pipeline Poisson noise (σ_{Poiss}). The orange line shows a standard normal distribution. **c,** Grey lines show the rms of model residuals versus bin size for all spectroscopic phase curves. The red line shows how the root-mean-square (rms) of the model residuals would bin down for uncorrelated ('white') noise.

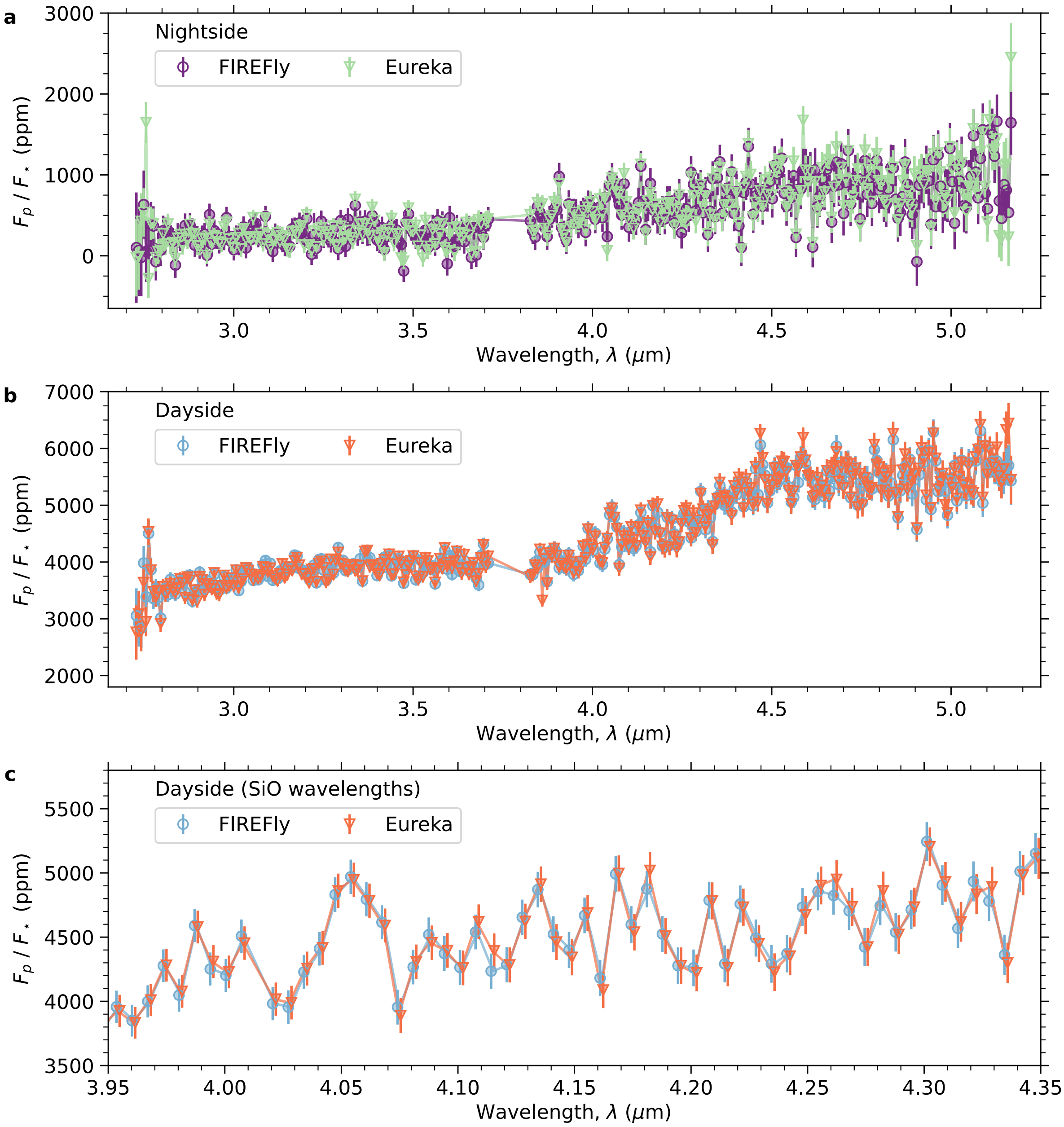

Supplementary Fig. 4 | Spectra obtained with independent data reductions. In our primary analysis, the raw data were reduced using the FIREFly pipeline. We also performed a second analysis, in which the independent Eureka! pipeline was used for the data reduction. **a,** A comparison of the resulting nightside ($n_\phi = 18$) emission spectra from FIREFly (purple circles) and Eureka! (green triangles). **b,** A comparison of the resulting dayside ($n_\phi = 34$) emission spectra from FIREFly (blue circles) and Eureka! (red triangles). **c,** The same as **b**, but displaying only the 3.95-4.35 µm wavelength range that encompasses the SiO signal. In **a-c**, data points show median values and error bars indicate standard deviations (1σ uncertainties) based on $n = 5{,}000$ posterior samples.

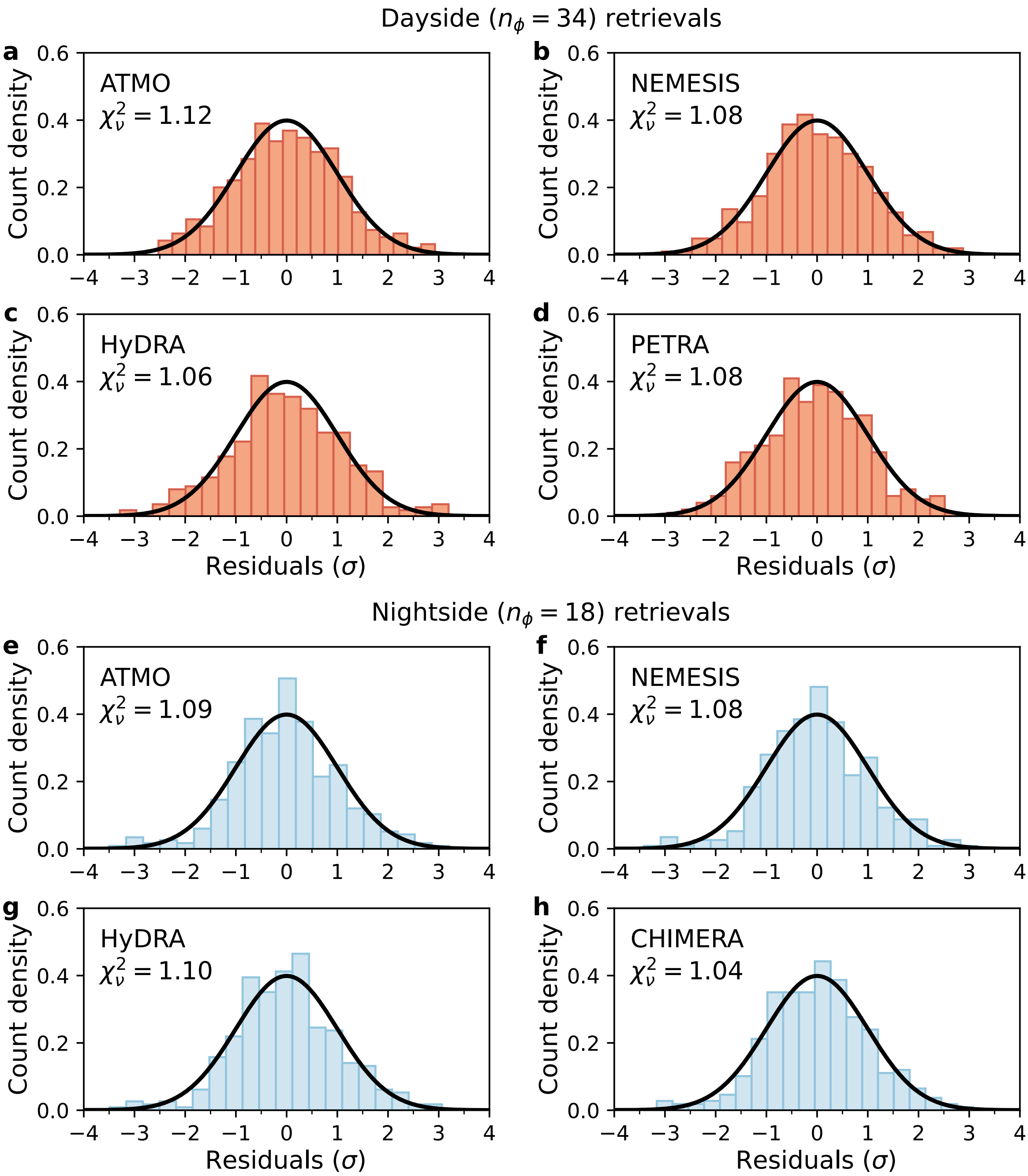

Supplementary Fig. 5 | Normalised residuals for the retrieval best-fit models. Histograms of residuals between the measured WASP-121b spectra and the best-fit retrieval models. Prior to binning, each residual was divided by the associated measurement uncertainty σ. Black lines show the standard normal distribution with zero mean and unity variance. Corresponding reduced chi-squared values (χ^2_υ) are printed in each panel (that is, the χ^2 fit metric divided by the number of degrees of freedom υ). **a-d**, Residuals obtained by ATMO, NEMESIS, HyDRA and PETRA for the dayside ($n_\phi = 34$) spectrum. **e-h**, Residuals obtained by ATMO, NEMESIS, HyDRA and CHIMERA for the nightside ($n_\phi = 18$) spectrum.

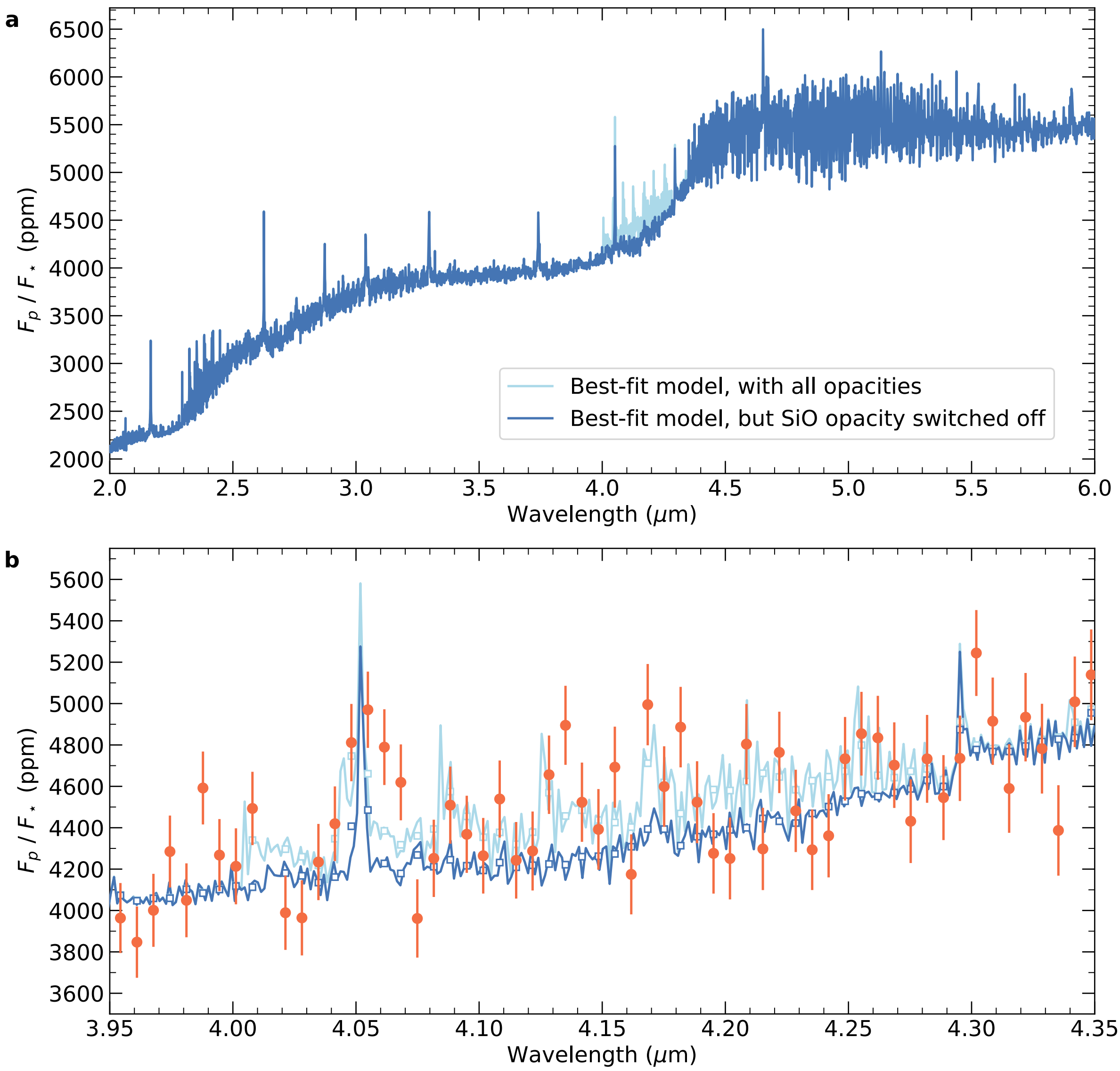

Supplementary Fig. 6 | SiO emission signal in the dayside spectrum of WASP-121b. a, The dark blue line shows the best-fit model obtained from the ATMO retrieval analysis, but with the SiO opacity switched off. The full best-fit model, including SiO opacity, is plotted underneath as a light blue line to highlight the SiO signal protruding across the 4.0-4.3 µm wavelength range. **b,** A zoom-in on the 4.0-4.3 µm wavelength range showing the same ATMO models as **a**, as well as the unbinned dayside emission data from Fig. 1 (red circles with error bars) and each model binned to the data wavelength channels (small squares).

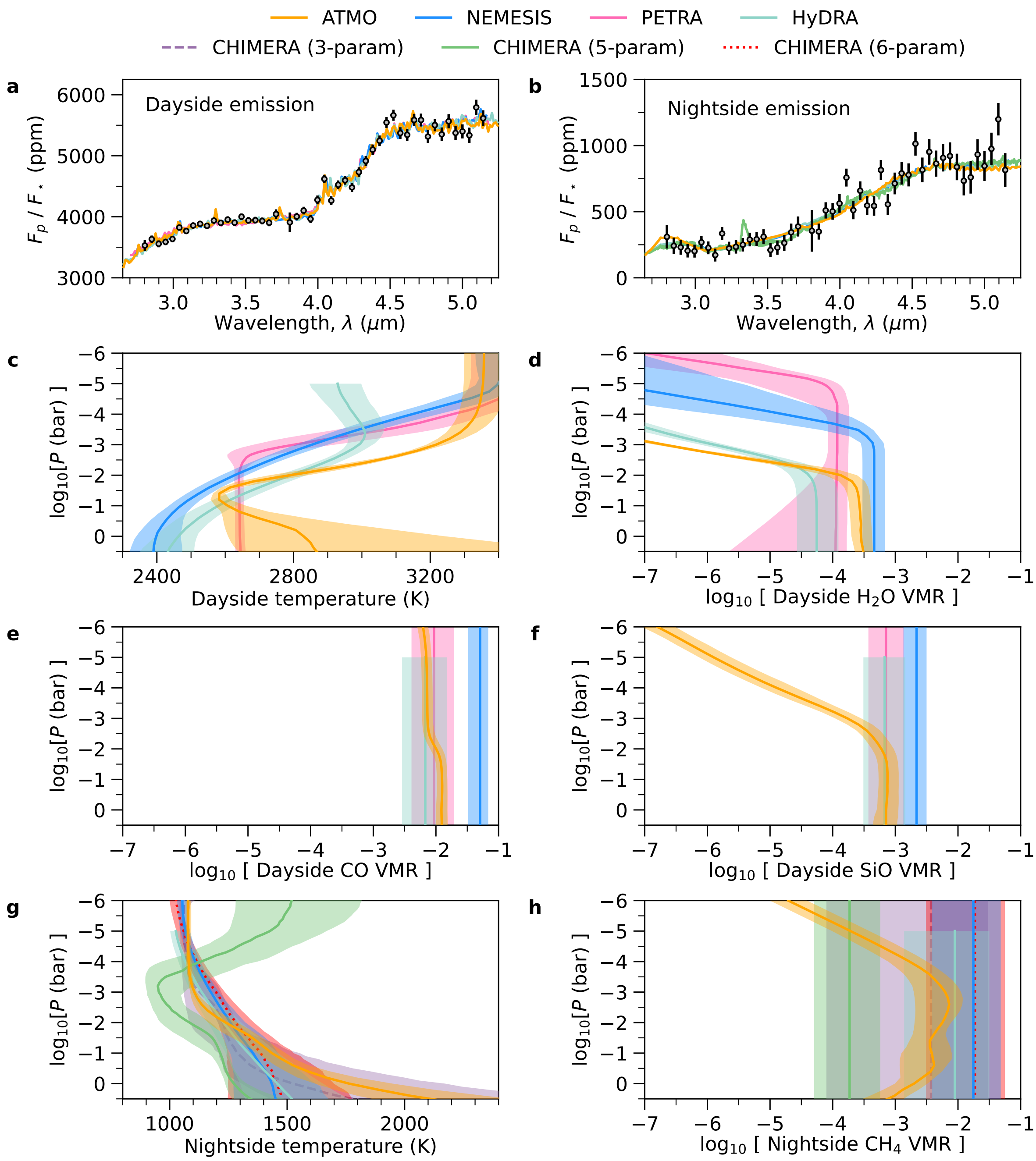

Supplementary Fig. 7 | Comparison of retrieval results. a-b, Black circles with grey filling show the binned emission measurements from Fig. 1 for the dayside ($n_\phi = 34$) and nightside ($n_\phi = 18$) hemispheres. Solid lines show the best-fit spectra from each retrieval code, with legend provided at the top of the figure. **c-h,** Inferred dayside PT profiles, dayside H_2O VMR profiles, dayside CO VMR profiles, dayside SiO VMR profiles, nightside PT profiles and nightside CH_4 VMR profiles. Lines show median values and shading indicates 1σ uncertainties defined by the 16th and 84th percentiles at each pressure level, based on at least $n = 1{,}000$ posterior samples in all cases. Note that the HyDRA models were evaluated down to a pressure of 10 µbar, while the other models were evaluated down to 1 µbar or lower.

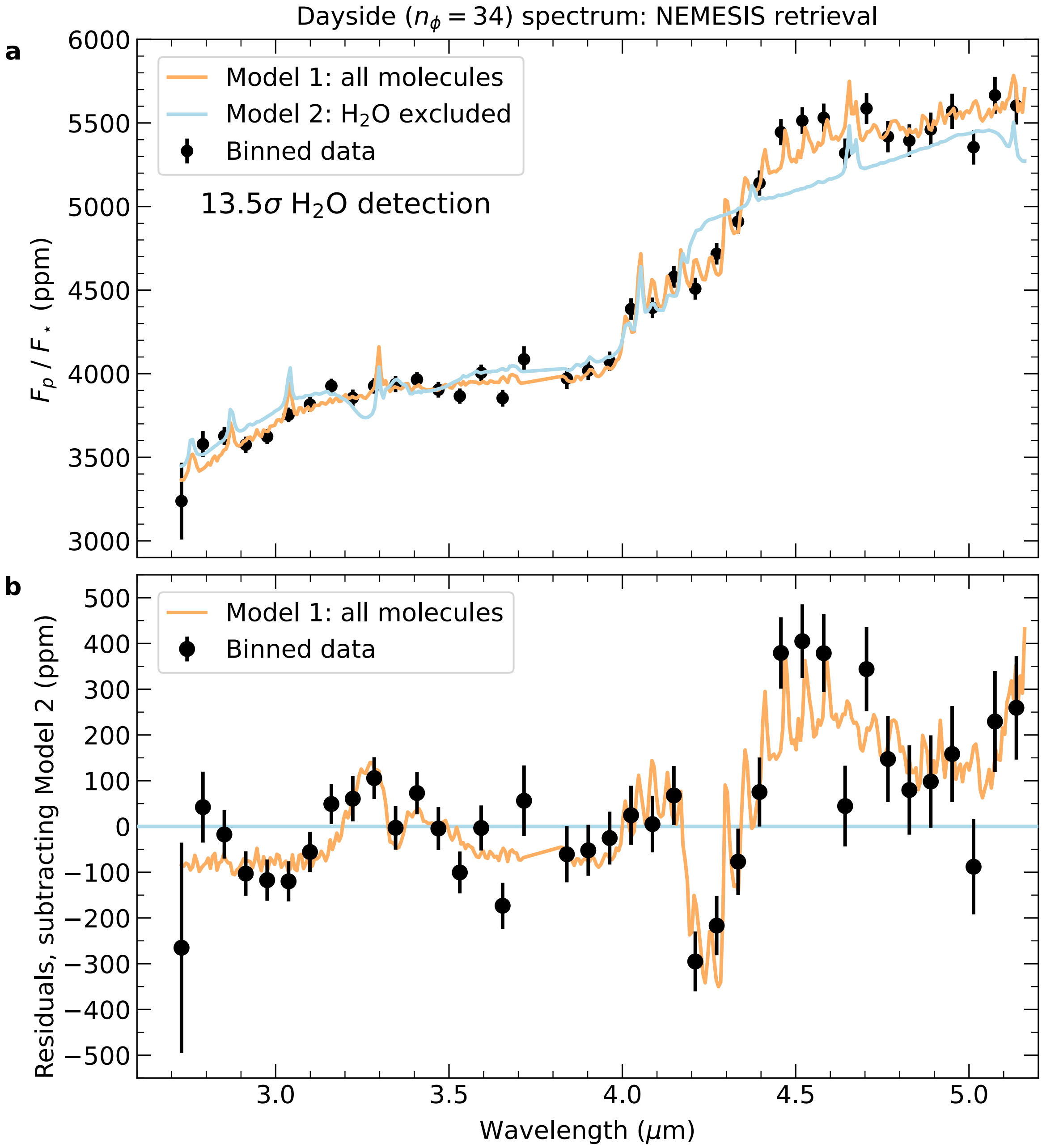

Supplementary Fig. 8 | NEMESIS dayside H_2O detection. a, Black circles show the measured WASP-121b dayside ($n_\phi = 34$) planet-to-star emission spectrum, binned in wavelength for visual clarity. The plotted values correspond to the median of the dayside emission measurements shown in Fig. 1, within each of 40 equally spaced wavelength bins. Error bars indicate $\tilde{\sigma}_j/\sqrt{N_j}$, where $\tilde{\sigma}_j$ is the median 1σ uncertainty and N_j is the number of points in the jth bin. The orange line shows the best-fit model obtained by NEMESIS with all chemical species considered, including H_2O (Model 1). The blue line shows the best-fit model obtained by NEMESIS for a separate retrieval using the same model setup, but with H_2O excluded as an opacity source (Model 2). As described in Methods, by comparing the Bayesian evidence of Models 1 and 2, the detection significance is determined to be 13.5σ. **b,** The same as **a** after subtracting Model 2 from both Model 1 and the data, to emphasise the wavelengths at which the inclusion of H_2O improves the fit to the data.

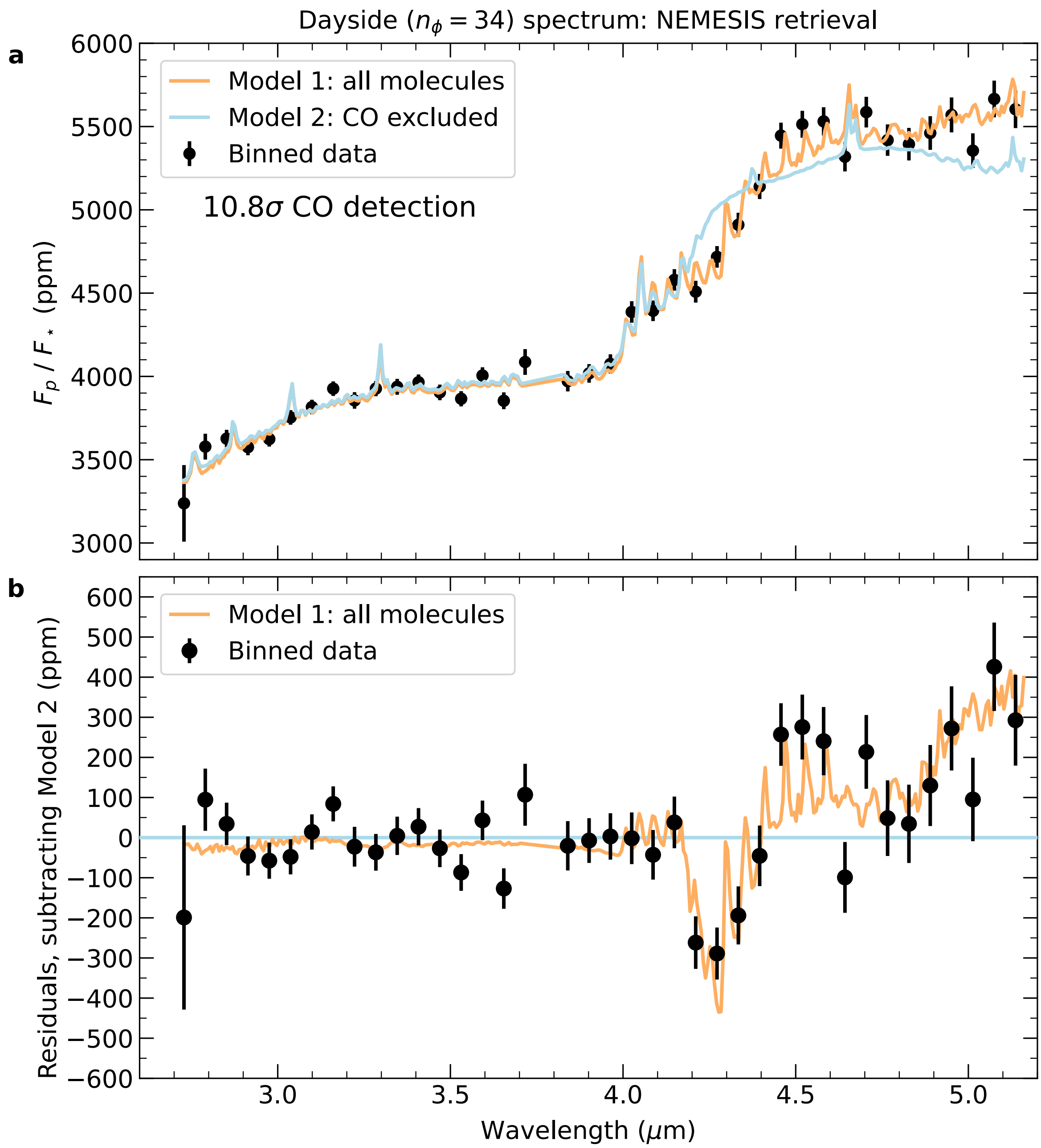

Supplementary Fig. 9 | NEMESIS dayside CO detection. The same as Supplementary Fig. 8 but showing the best-fit models for the WASP-121b dayside ($n_\phi = 34$) spectrum obtained by NEMESIS with and without CO.

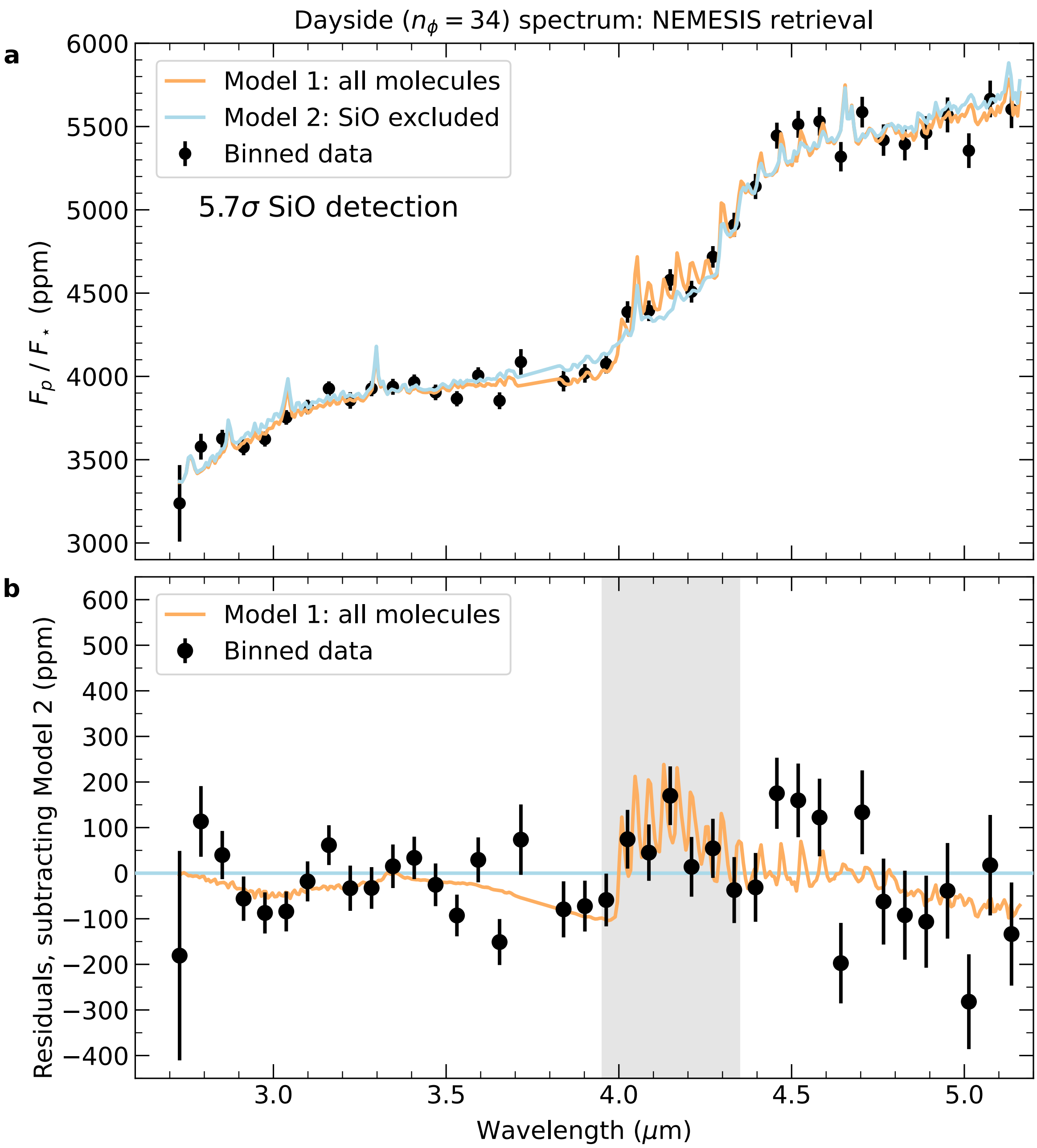

Supplementary Fig. 10 | NEMESIS dayside SiO detection. The same as Supplementary Fig. 8 but showing the best-fit models for the WASP-121b dayside ($n_\phi = 34$) spectrum obtained by NEMESIS with and without SiO.

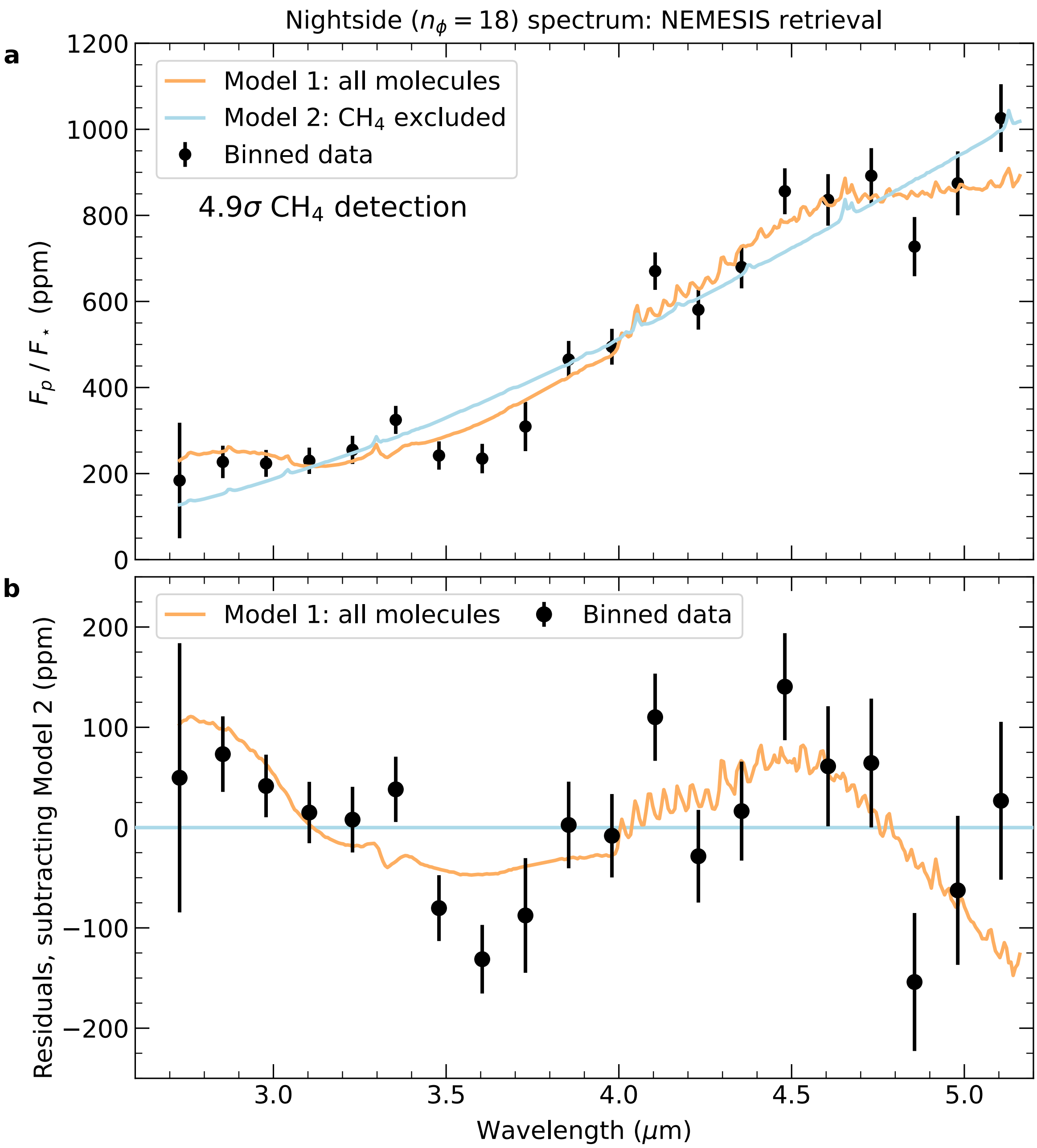

Supplementary Fig. 11 | NEMESIS nightside CH_4 detection. The same as Supplementary Fig. 8 but showing the best-fit models for the WASP-121b nightside ($n_\phi = 18$) spectrum obtained by NEMESIS with and without CH_4. Rather than 40 bins, only 20 bins have been used due to the relatively low signal-to-noise of the nightside spectrum compared to the dayside spectrum.

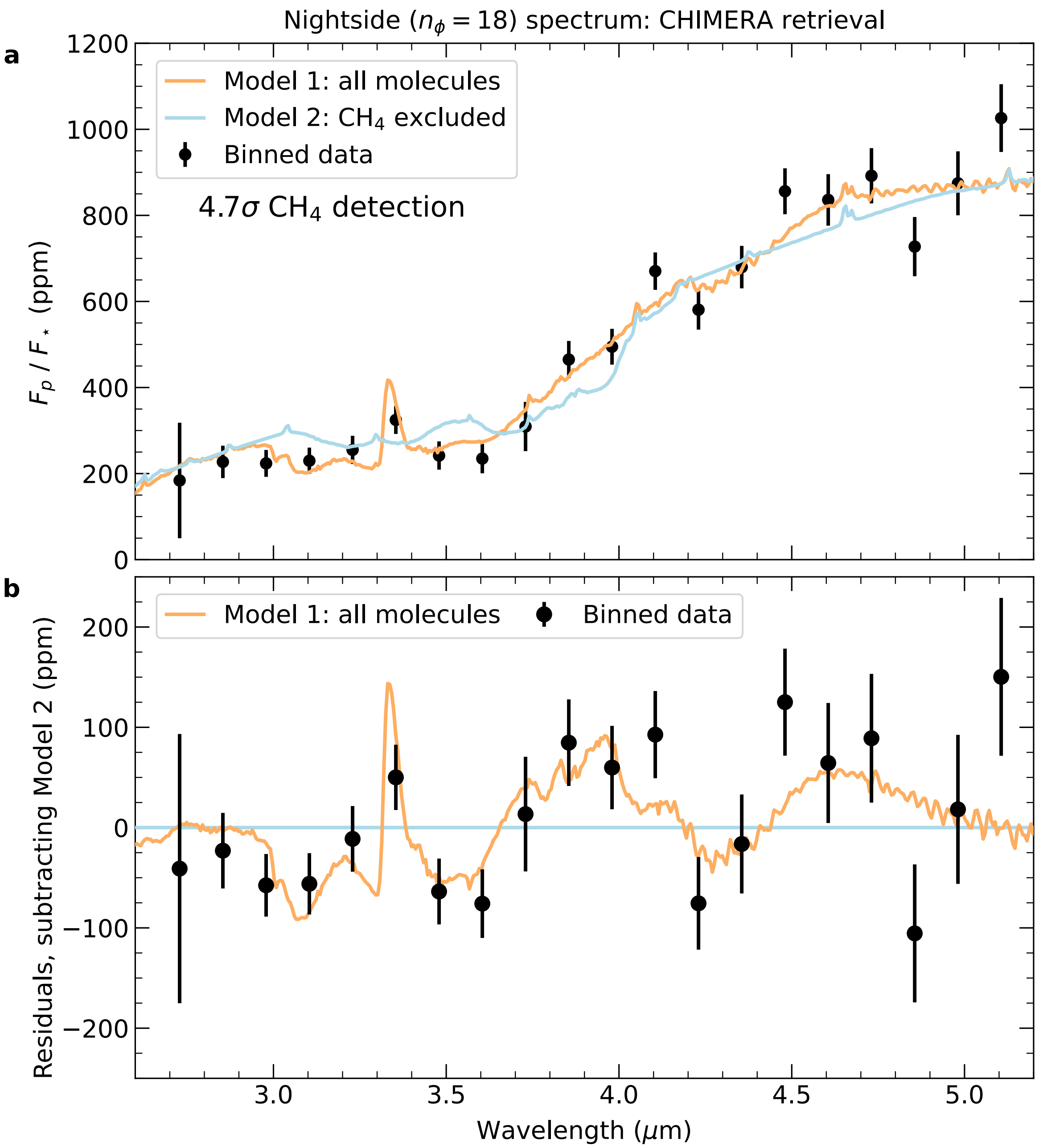

Supplementary Fig. 12 | CHIMERA nightside CH_4 detection. The same as Supplementary Fig. 11 but showing the best-fit models for the WASP-121b nightside (n_ϕ = 18) spectrum obtained by CHIMERA with and without CH_4.

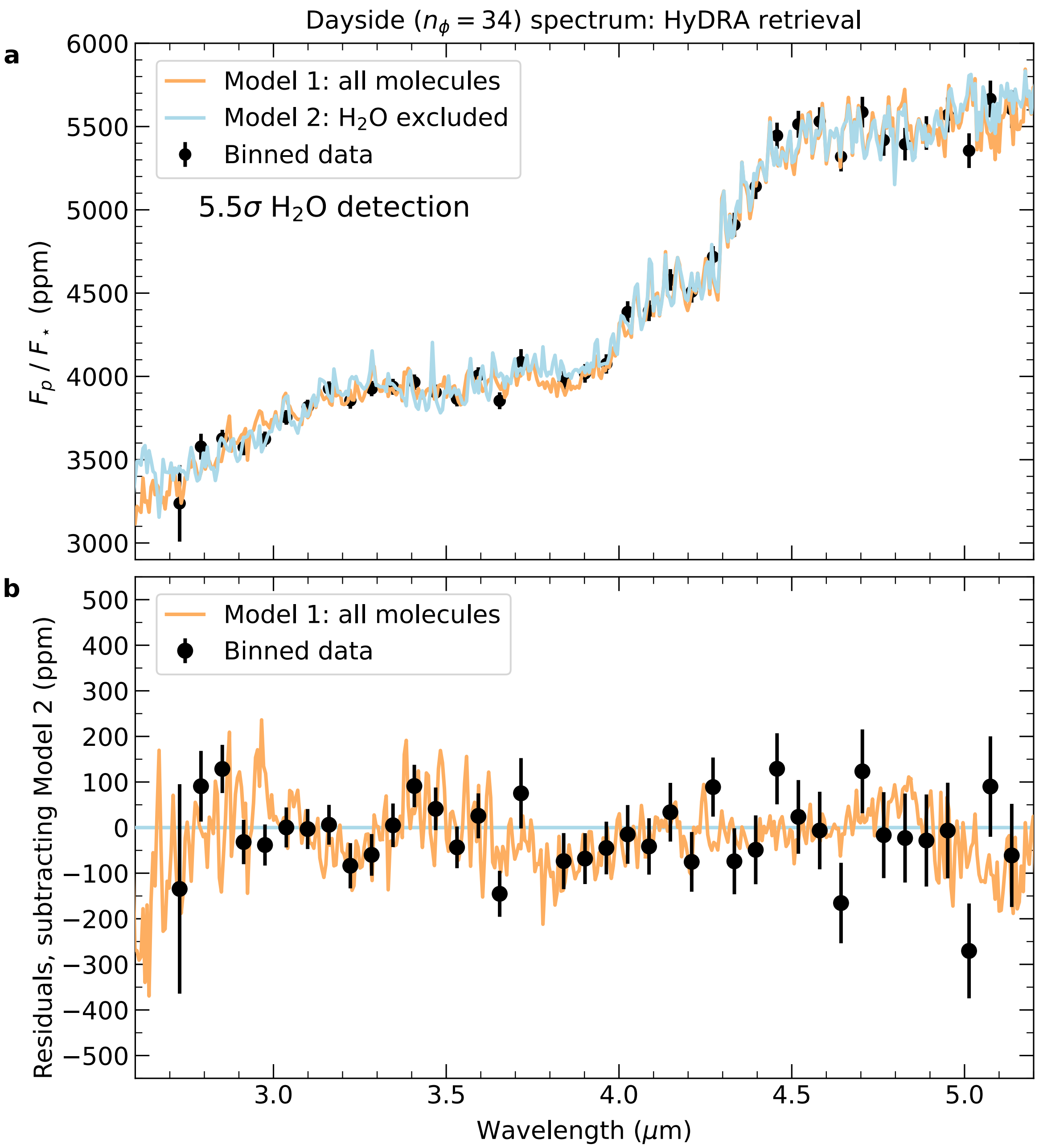

Supplementary Fig. 13 | HyDRA dayside H_2O detection. The same as Supplementary Fig. 8 but showing the best-fit models for the WASP-121b dayside ($n_\phi = 34$) spectrum obtained by HyDRA with and without H_2O.

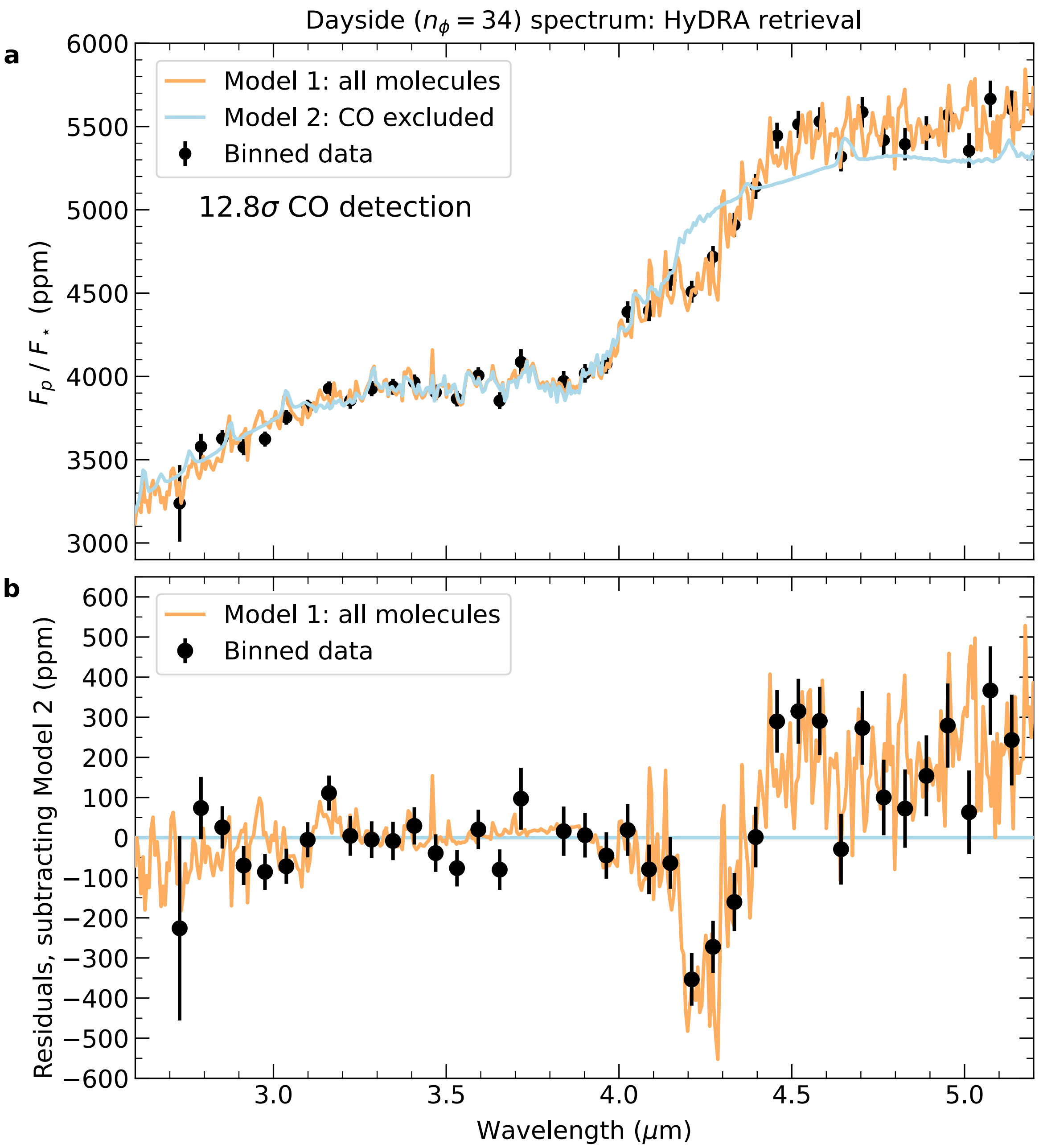

Supplementary Fig. 14 | HyDRA dayside CO detection. The same as Supplementary Fig. 8 but showing the best-fit models for the WASP-121b dayside ($n_\phi = 34$) spectrum obtained by HyDRA with and without CO.

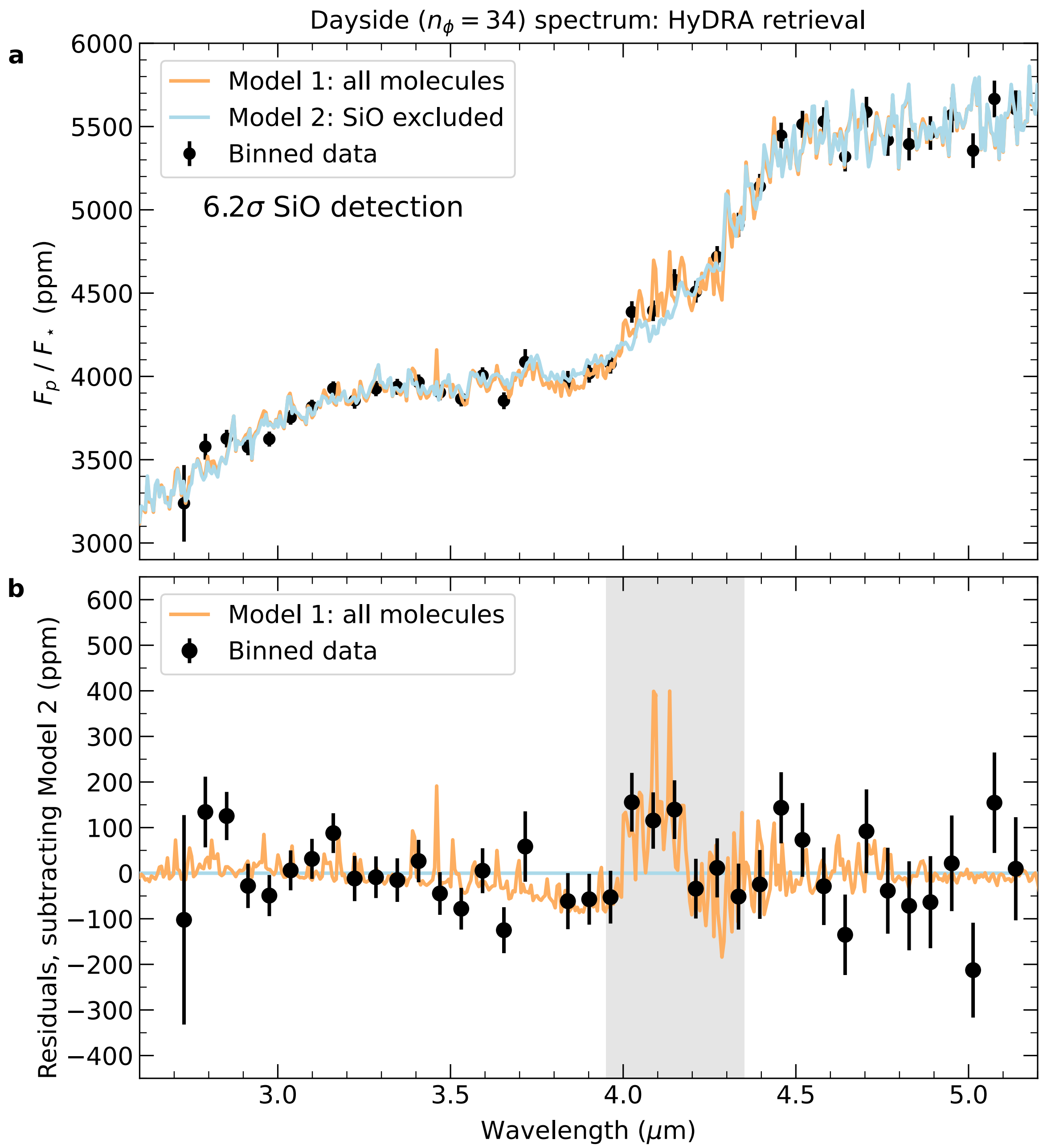

Supplementary Fig. 15 | HyDRA dayside SiO detection. The same as Supplementary Fig. 8 but showing the best-fit models for the WASP-121b dayside ($n_\phi = 34$) spectrum obtained by HyDRA with and without SiO.

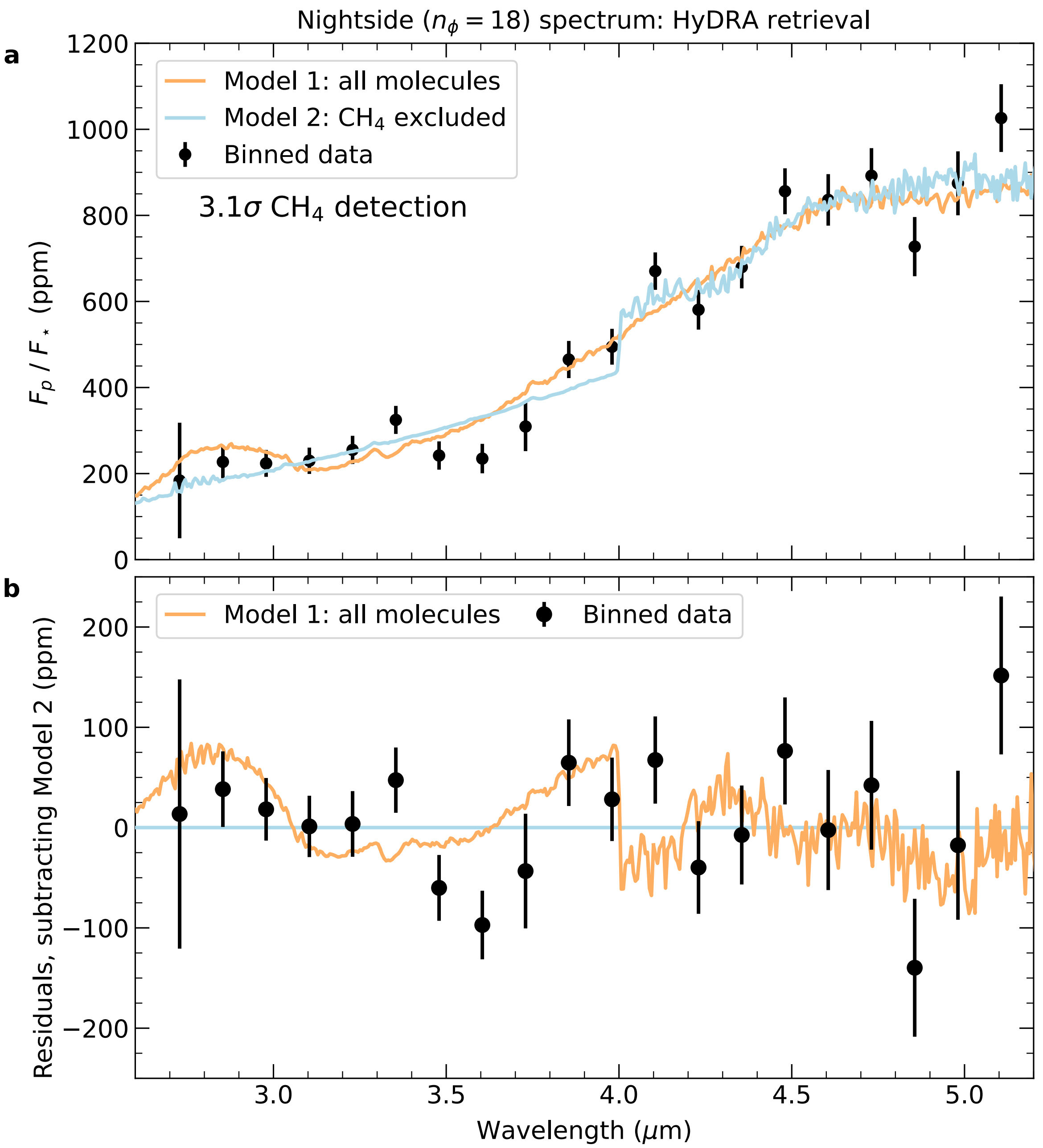

Supplementary Fig. 16 | HyDRA nightside CH_4 detection. The same as Supplementary Fig. 11 but showing the best-fit models for the WASP-121b nightside ($n_\phi = 18$) spectrum obtained by HyDRA with and without CH_4.

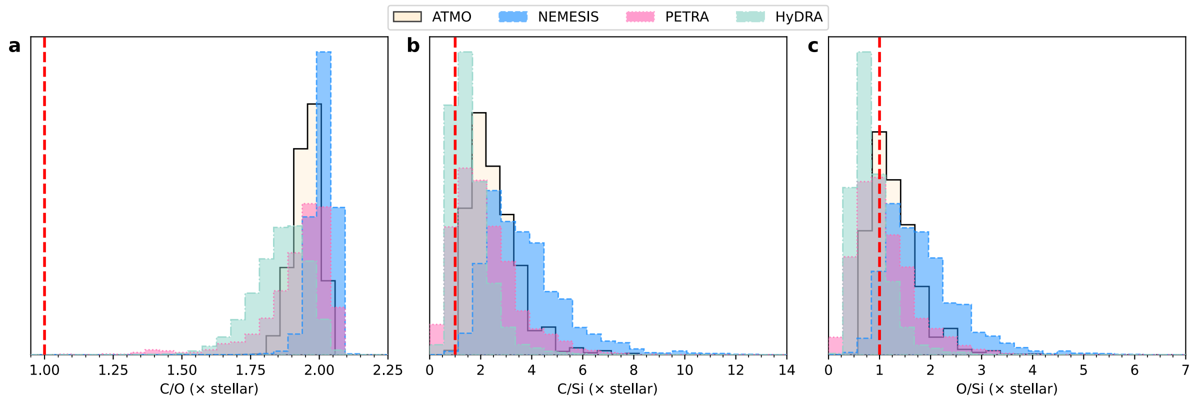

Supplementary Fig. 17 | Element abundance ratios across retrievals. Posterior distributions obtained for the **a**, C/O, **b**, C/Si, and **c,** O/Si ratios of the planetary atmosphere relative to the corresponding stellar ratio, as obtained from the dayside retrieval analyses. Vertical dashed lines in each panel coincide with a planetary value equal to the stellar value, where stellar abundance ratios were derived from high-resolution spectroscopy (see 'Stellar abundances and relative planetary abundances' in the Methods).

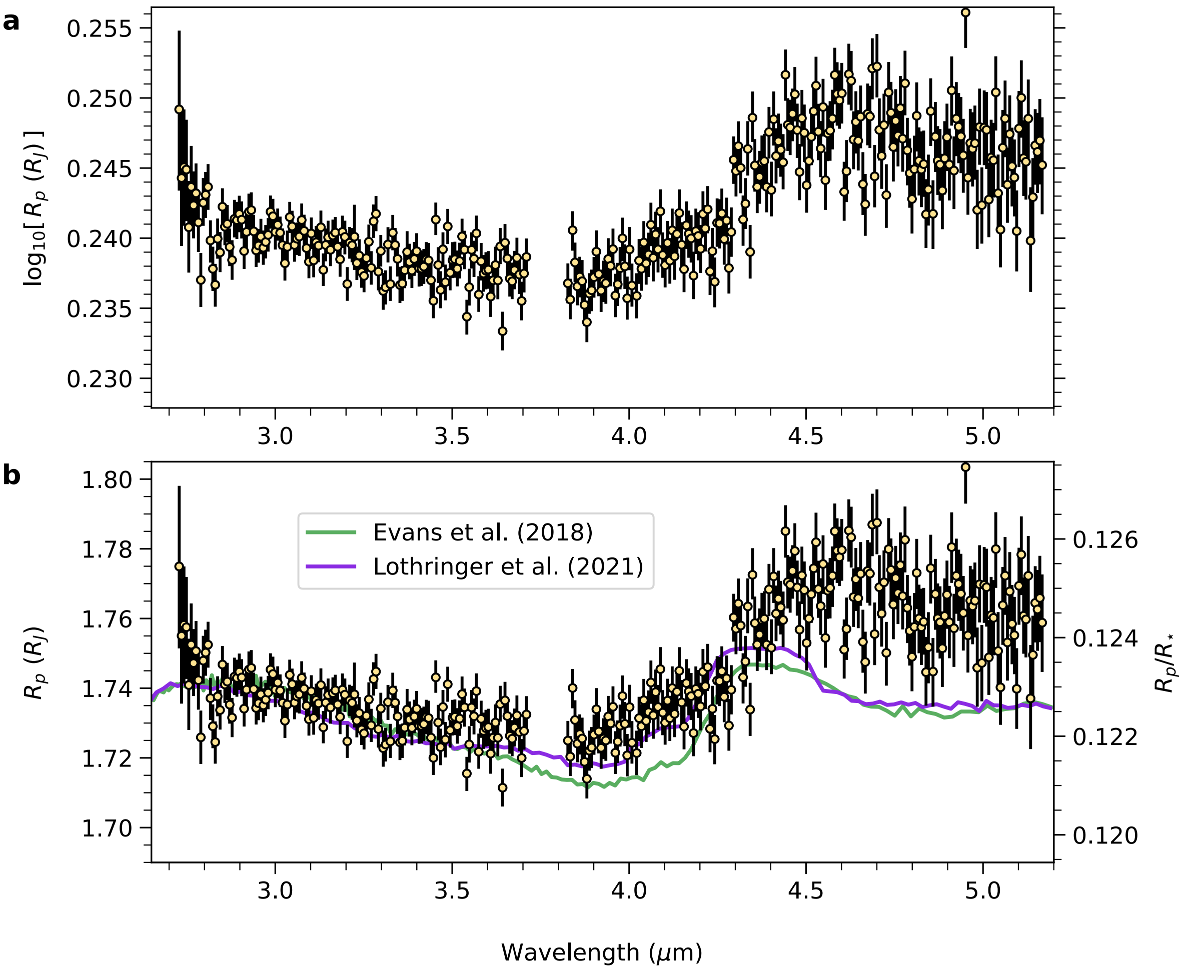

Supplementary Fig. 18 | Planetary radius for each wavelength channel. Circles show median values and error bars indicate 1σ uncertainties defined by the 16th and 84th percentiles of $n = 5{,}000$ posterior samples for each of the 349 spectroscopic phase-curve fits. **a,** Wavelength-dependent values for $\log_{10}[R_\mathrm{p}\ (R_\mathrm{J})]$ obtained directly from the spectroscopic phase-curve fits, where R_J denotes the radius of Jupiter. **b,** Wavelength-dependent values for R_p in units of Jupiter radii, derived from the $\log_{10}[R_\mathrm{p}\ (R_\mathrm{J})]$ values. The right vertical axis displays the corresponding planet-to-star radius ratio ($R_\mathrm{p}/R_\star$). Models from ref. [1] (purple line) and ref. [167] (green line) are also shown, both of which were obtained by fitting to HST data at shorter wavelengths and have not been fitted to the JWST data.

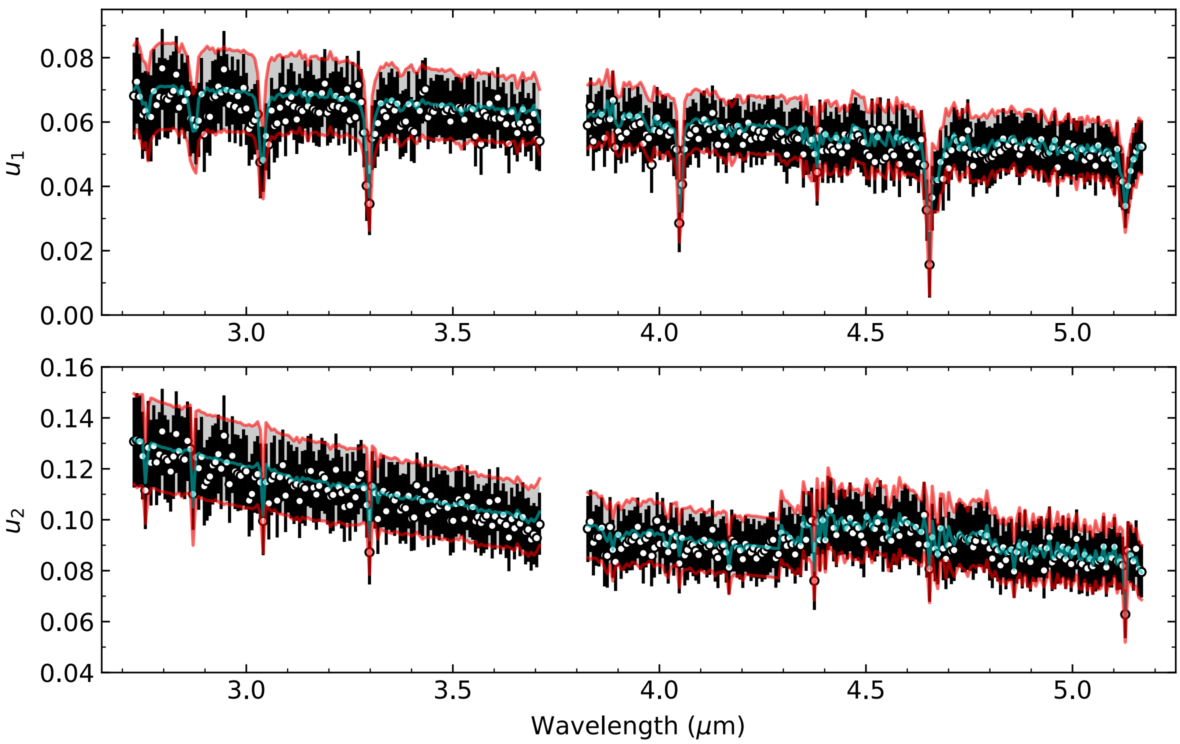

Supplementary Fig. 19 | Stellar limb darkening. Inferred coefficients u_1 (top panel) and u_2 (bottom panel) for the quadratic stellar limb-darkening law adopted in the phase-curve fits. In both panels, circles show median values and error bars indicate 1σ uncertainties defined by the 16th and 84th percentiles of $n = 5{,}000$ posterior samples for each of the 349 spectroscopic phase-curve fits. Light blue lines show the mean values and grey shaded regions with red boundaries indicate the standard deviations of the ExoTiC-LD normal priors adopted for each wavelength channel.

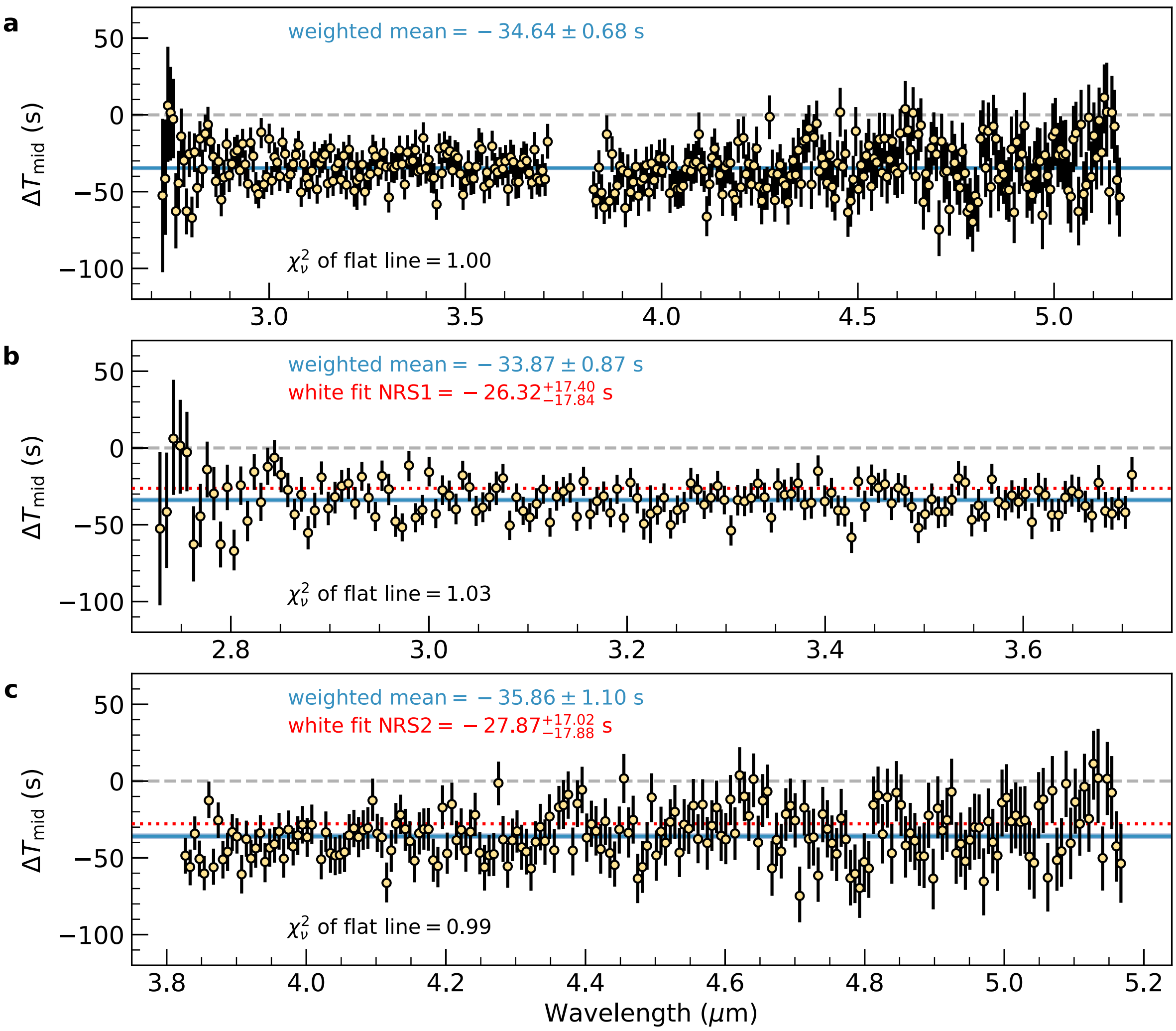

Supplementary Fig. 20 | Transit mid-time offsets for each wavelength channel. a, Measured transit mid-time offsets ($\Delta T_{\rm mid}$) relative to the transit mid-time reported in ref. [51], across the full G395H wavelength range. Circles show median values and error bars indicate 1σ uncertainties defined by the 16th and 84th percentiles of $n = 5{,}000$ posterior samples for each of the 349 spectroscopic phase-curve fits. **b-c,** The same as **a** but only showing the wavelength ranges of the NRS1 and NRS2 detectors. In each panel, the weighted-mean of the plotted data with uncertainty given by the associated standard deviation is printed in blue font at the top of the axis and plotted as a horizontal blue line. For the NRS1 and NRS2 panels, the values obtained from the white phase-curve fit (Supplementary Table 1) are displayed in red font for comparison and plotted as dotted red lines. Reduced chi-squared values (χ^2_ν) calculated under the assumption of $\Delta T_{\rm mid}$ being constant (but not necessarily zero) at all wavelengths are printed at the bottom of each panel in black font. Dashed grey lines indicate $\Delta T_{\rm mid} = 0$ for reference.

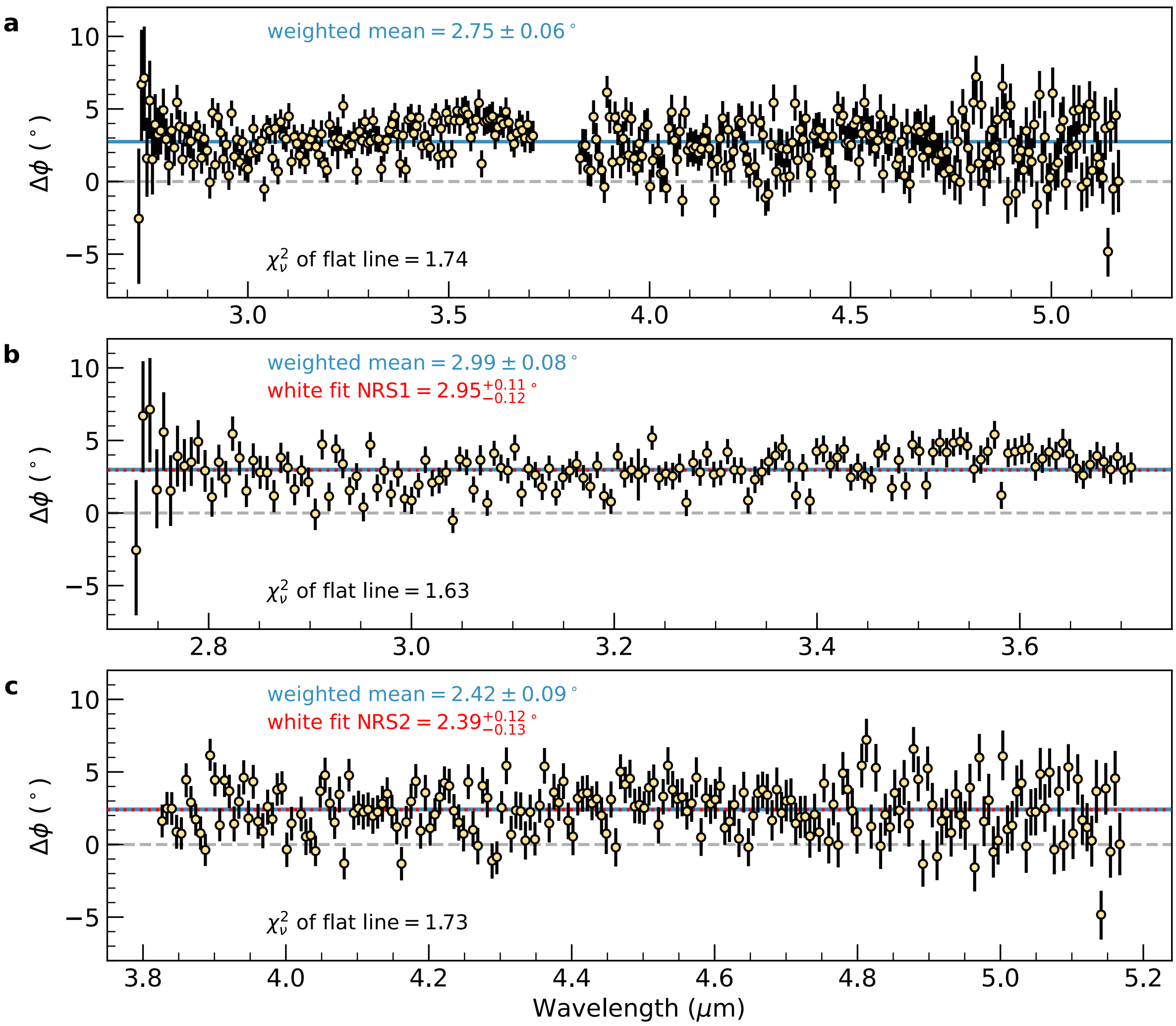

Supplementary Fig. 21 | Planetary brightness map phase offsets for each wavelength channel. Similar to Supplementary Fig. 20 but showing the measured planetary brightness map phase offsets ($\Delta\phi$).